Exploring valence-electron dynamics of xenon through laser-induced electron diffraction

Fang Liu,[1,2,3,*] Slawomir Skruszewicz,[4] Julian Späthe,[5] Yinyu Zhang,[5] Sebastian Hell,[5] Bo Ying,[5,1] Gerhard G. Paulus,[5,1] Bálint Kiss,[6] Krishna Murari,[6] Malin Khalil,[6] Eric Cormier,[6] Li Guang Jiao,[2,7] Stephan Fritzsche,[1,2,3] and Matthias Kübel[1,5,†]

[1]*Helmholtz-Institut Jena, 07743 Jena, Germany*
[2]*Theoretisch-Physikalisches Institut, Friedrich-Schiller-Universität Jena, 07743 Jena, Germany*
[3]*GSI Helmholtzzentrum für Schwerionenforschung GmbH, 64291 Darmstadt, Germany*
[4]*Deutsches Elektronen-Synchrotron DESY, Notkestr. 85, 22607 Hamburg, Germany*
[5]*Institute of Optics and Quantum Electronics, 07743 Jena, Germany*
[6]*ELI-ALPS, ELI-HU Non-Profit Ltd., Wolfgang Sandner utca 3., Szeged, H-6728, Hungary*
[7]*College of Physics, Jilin University, Changchun 130012, People's Republic of China*

(Received 18 March 2024; revised 28 June 2024; accepted 2 July 2024; published 22 July 2024)

Strong-field ionization can induce electron motion in both the continuum and valence shell of the parent ion. Here we report on a joint theoretical and experimental investigation of laser-induced electron diffraction in xenon. We explore the interplay of electron recollision with spin-orbit dynamics in the valence shell of the xenon cation. On the theory side, the electron-hole potentials for two different states are constructed, and the quantitative rescattering model is used to calculate the photoelectron momentum distributions (PMDs) for high-order above-threshold ionization of xenon. Measurements were carried out using 40-fs laser pulses with a central wavelength of 3100 nm and a peak laser intensity of 6×10^{13} W/cm^2. The simulated PMDs describe well the features of the measured angular distributions of photoelectrons. Our study reveals a theoretical distinction between the electron signals resulting from rescattering off the $m = 0$ and $|m| = 1$ hole states, particularly noting a distinct change along the backward scattering angles. However, to fully identify the contributions of the hole states, a more accurate agreement between theory and experiment will be needed.

DOI: 10.1103/PhysRevA.110.013118

I. INTRODUCTION

Laser-induced electron diffraction (LIED) has been established as a powerful alternative to conventional electron diffraction; see Refs. [1,2] for recent reviews. The technique relies on the laser-driven elastic rescattering [3] of a photoelectron emitted by strong-field ionization, which gives rise to high-order above threshold ionization (HATI), the basic strong-field phenomenon underlying LIED. The rescattering process provides LIED with two interesting properties: first, an ultrahigh current density, allowing imaging on the single-molecule level [4] and, second, perfect synchronization between ionization and scattering events, allowing (attosecond) time-resolved experiments [5–7].

The LIED signal can be described by the atomic scattering cross sections and a molecular interference term [4,8,9]. Numerous LIED experiments have focused on the measurement of the molecular interference term, and the accurate, and time-dependent, retrieval of molecular bond lengths has been demonstrated [6,7,10]. Notably, these measurements require the recolliding electron to possess a sufficiently short de Broglie wavelength and correspondingly large momentum. For this reason, long driving wavelengths ($\lambda \gtrsim 2$ m) are favorable to drive LIED experiments for molecular structure retrieval. In the case of atoms or lower recollision momentum, the scattering signal is governed by the differential elastic electron scattering cross sections (DCSs), which depend on the valence electron distribution [11]. Good agreement between measured LIED patterns and DCSs known from conventional electron diffraction experiments has been obtained [12,14].

Specifically, strong-field driven tunnel ionization is not only the primary step in HATI and LIED but can also initiate electronic and nuclear dynamics inside the parent ion, thus acting as a "pump." This has enabled ultrastable pump-probe-type experiments: attosecond time resolution is obtained by exploiting the perfect synchronization between the laser field and the recolliding electron [3]. As the returning electron wave packet is chirped, an energy-resolved measurement of the returning electron, acting as a probe, provides access to different pump-probe delays. This principle has been exploited for time-resolved measurements of nuclear dynamics in high-harmonic spectroscopy [15,16] and LIED experiments [6,7]. While the prospect of employing high-harmonic generation (HHG) for probing [15,17] is inherently appealing, a significant challenge arises from the strong impact of phase matching on HHG [18–20]. In contrast, LIED is insensitive to phase matching, representing a promising alternative. However, to the best of our knowledge, LIED experiments revealing electron-hole dynamics have not yet been reported.

*Contact author: fang.liu@uni-jena.de
†Contact author: matthias.kuebel@uni-jena.de

 ©2024 American Physical Society

Here we study the interplay of continuum and bound electron dynamics in the HATI process. Our approach is best illustrated by viewing laser-induced recollision as a pump-probe experiment [21,22]: tunnel ionization takes the role of a pump pulse which essentially starts two clocks: a laser-dependent one that corresponds to the field-driven motion of free electrons undergoing elastic rescattering, and a target-dependent one that relates to the bound electron dynamics. Both clocks are read at the time of recollision when the recolliding electron probes the hole density of the ion by elastic scattering.

In this work we consider the xenon (Xe) atom. The ground state of the Xe cation has two fine-structure components: the $^2P_{3/2}$ and $^2P_{1/2}$ that are separated by $\Delta E_{\mathrm{SO}} = 1.3\,\mathrm{eV}$ due to spin-orbit interaction. Both ion states are coherently populated by tunnel ionization, thus creating a wave packet [13]. As the spin-orbit wave packet evolves, the $5p^5$ electron-hole (vacancy) in the valence shell oscillates between the $m = 0$ state and the $|m| = 1$ (m is the magnetic quantum number) states of the valence shell of the Xe^+ ion with the period $T_{\mathrm{SO}} = h/\Delta E_{\mathrm{SO}}$ (3.2 fs) [23]. The spatial hole density in the valence shell is described by the orbitals for $m = 0$ ("peanut shape") and $|m| = 1$ ("donut shape"). At integer n and half-integer $(n + \frac{1}{2})$ multiples of the spin-orbit period (where $n = 0, 1, 2, 3, \ldots$), the hole alternately populates the $m = 0$ and $|m| = 1$ orbitals, respectively. The oscillating hole density has been tracked in Kr using attosecond transient spectroscopy [24]. For the Ne and Ar ion momentum spectroscopy [25] or momentum imaging of direct electrons [26,27] has been applied. Recently, the spin-orbit wave packet in Xe has been probed using sequential double ionization in an elliptically polarized near-infrared laser field [28]. Here we employ elastic rescattering in a midinfrared field ($\lambda = 3100\,\mathrm{nm}$) with an optical period of $T = 10.5$ fs. Owing to the relatively long optical period, the returning electron wave packet spans several femtoseconds, allowing us, in principle, to probe the evolution of the spin-orbit wave packet in xenon.

The article is structured as follows. In Sec. II the theoretical model is introduced, including the strong-field approximation. We describe the method to construct the electron-hole potential and outline the quantitative rescattering theory (QRS) model used to calculate the photoelectron momentum distributions (PMDs) for HATI. Based on the QRS model, the simulated results are shown and discussed in Sec. III. Finally, Sec. IV contains conclusions and outlook.

Unless indicated otherwise, atomic units ($m_e = e = \hbar = 4\pi\varepsilon_0 = 1$) are used throughout the paper.

II. THEORETICAL MODEL

A. The strong-field approximation

In the strong-field approximation (SFA) [29,30], the first two terms of the perturbation series, called direct (SFA1) and rescattering (SFA2) amplitudes, respectively, express the momentum-dependent ionization amplitude as

$$f_{\mathrm{SFA}}(\boldsymbol{p}) = f_{\mathrm{SFA1}}(\boldsymbol{p}) + f_{\mathrm{SFA2}}(\boldsymbol{p}), \tag{1}$$

where $\boldsymbol{p}$ is the momentum of the detected photoelectron. The direct ionization amplitude in Eq. (1) is given by

$$f_{\mathrm{SFA1}}(\boldsymbol{p}) = -i\int_{-\infty}^{\infty} dt\,\langle\chi_{\boldsymbol{p}}(t)|\boldsymbol{r}\cdot\boldsymbol{F}(t)|\Psi_i(t)\rangle, \tag{2}$$

where $\boldsymbol{F}(t) = -\partial\boldsymbol{A}(t)/\partial t$ is the laser electric field, and $\Psi_i(t)$ is the initial ground state wave function. The Volkov state $\chi_{\boldsymbol{p}}(t)$ in Eq. (2) is given by

$$\langle\boldsymbol{r}|\chi_{\boldsymbol{p}}(t)\rangle = \frac{1}{(2\pi)^{3/2}} e^{i[\boldsymbol{p}+\boldsymbol{A}(t)]\cdot\boldsymbol{r}} e^{-iS(\boldsymbol{p},t)}, \tag{3}$$

where the action S reads as

$$S(\boldsymbol{p},t) = \frac{1}{2}\int_{-\infty}^{t} dt'[\boldsymbol{p}+\boldsymbol{A}(t')]^2. \tag{4}$$

The second term in Eq. (1), the so-called rescattering amplitude, accounts for laser-induced elastic scattering of the returning electron from the parent ion. This rescattering amplitude can be expressed as

$$f_{\mathrm{SFA2}}(\boldsymbol{p}) = -\int_{-\infty}^{\infty} dt\int_{t}^{\infty} dt'\int d\boldsymbol{k}\langle\chi_{\boldsymbol{p}}(t')|V|\chi_{\boldsymbol{k}}(t')\rangle \times\langle\chi_{\boldsymbol{k}}(t)|\boldsymbol{r}\cdot\boldsymbol{F}(t)|\Psi_i(t)\rangle, \tag{5}$$

where V is the scattering potential. It takes the form

$$V(r) = \widetilde{V}(r)e^{-\alpha r}, \tag{6}$$

where α is a screening factor introduced to avoid the singularity in the integrand in Eq. (5) and $\widetilde{V}(r)$ is the atomic model potential that can be written in the form

$$\widetilde{V}(r) = -\frac{1 + a_1 e^{-a_2 r} + a_3 r e^{-a_4 r} + a_5 e^{-a_6 r}}{r}. \tag{7}$$

The parameters $a_i (i = 1, 3, 5)$ can be found in Ref. [31]. As can be seen from Eq. (5), the rescattering amplitude involves three steps by the electron under laser field: the initial tunnel ionization, propagation in the laser field, as well as elastic scattering with the parent ion.

B. Elastic differential cross sections

In this section we briefly summarize the standard potential scattering theory, which has been well documented in the textbook [32]. The scattered wavefunction of an electron by a spherical potential $V(r)$ satisfies the time-independent Schrödinger equation

$$[\nabla^2 + k^2 - U(r)]\psi(\boldsymbol{r}) = 0, \tag{8}$$

where $U(r) = 2V(r)$ is the reduced potential and k is the electron momentum, related to the electron energy by $k = \sqrt{2E}$. For a short-range potential which falls faster than r^{-2} as $r \to \infty$, the wave function of the scattered electron in the asymptotic region is given by

$$\psi^+(\boldsymbol{r})_{r\to\infty} = \frac{1}{(2\pi)^{3/2}}\left[e^{i\boldsymbol{k}\cdot\boldsymbol{r}} + f(\theta)\frac{e^{ikr}}{r}\right], \tag{9}$$

where $f(\theta)$ is the scattering amplitude and θ is the polar angle measured from the incident direction.

To obtain the scattering amplitude, we solve Eq. (8) by expanding the scattered wave function in partial waves,

$$\psi^{+}(\boldsymbol{r}) = \sqrt{\frac{2}{\pi}}\frac{1}{kr}\sum_{lm} i^{l} u_l(k,r) Y_{lm}(\hat{\boldsymbol{r}}) Y^{*}_{lm}(\hat{\boldsymbol{k}}), \tag{10}$$

where Y_{lm} is a spherical harmonic. The continuum waves are normalized to $\delta(\boldsymbol{k}-\boldsymbol{k}')$. The radial equation $u_l(k,r)$ satisfies

$$\left[\frac{d^2}{dr^2} + k^2 - \frac{l(l+1)}{r^2} - U(r)\right] u_l(k,r) = 0. \tag{11}$$

For a plane wave when $V(r)=0$, the radial component $u_l(k,r)/kr$ in Eq. (10) is a standard spherical Bessel function $j_l(kr)$.

When $r\to\infty$, the boundary condition satisfied by $u_l(k,r)$ for $V(r)=0$ is

$$u_l(k,r) = \sin\left(kr - \tfrac{1}{2}l\pi\right), \tag{12}$$

while for a short-range potential $V(r)$,

$$u_l(k,r) = e^{(i\delta_l)}\sin\left(kr - \tfrac{1}{2}l\pi + \delta_l\right), \tag{13}$$

where δ_l is a phase shift that displays the influence of the interaction.

By matching the coefficients of the outgoing spherical waves in Eqs. (9) and (10), and using Eqs. (12) and (13), the scattering amplitude is given by

$$f(\theta) = \sum_{l=0}^{\infty}\frac{2l+1}{k} e^{\mathrm{i}\delta_l}\sin(\delta_l) P_l(\cos\theta), \tag{14}$$

where $P_l(\cos\theta)$ are the Legendre polynomials.

The scattering by a Coulomb potential,

$$V_c(r) = \frac{Z_1 Z_2}{r}, \tag{15}$$

where Z_1 and Z_2 are the charges of the projectile and the target, can be treated in parabolic coordinates and the scattering amplitude can be obtained analytically,

$$f_c(\theta) = -\eta e^{2\mathrm{i}\sigma_0}\frac{e^{-\mathrm{i}\eta\ln[\sin^2(\theta/2)]}}{2k\sin^2(\theta/2)}, \tag{16}$$

where

$$\sigma_0 = -\arg[\Gamma(1+\mathrm{i}\eta)], \quad \eta = \frac{Z_1 Z_2}{k}. \tag{17}$$

In order to mimic the partial screening of the nuclear charge by the electrons, a short-range potential $V(r)$ is added to a Coulomb potential $V_c(r)$, using partial-wave expansion. The scattering amplitude for $V(r)$ can be expressed by

$$\hat{f}(\theta) = \sum_{l=0}^{\infty}\frac{2l+1}{k} e^{2\mathrm{i}\sigma_l} e^{\mathrm{i}\delta_l}\sin(\delta_l) P_l(\cos\theta). \tag{18}$$

Thus, the scattering amplitude for the general case is given by

$$f(\theta) = f_c(\theta) + \hat{f}(\theta), \tag{19}$$

and the elastic scattering DCS for a given energy reads

$$\frac{d\sigma_{el}(k,\theta)}{d\Omega_r} = |f(\theta)|^2. \tag{20}$$

C. The electron-hole potential

Here the scattering potentials used in the numerical calculations are given. We consider the elastic scattering of electrons with the Xe^+ ion. The DCSs for the $m=0$ and $|m|=1$ vacancy states are calculated using standard potential scattering theory, as detailed above.

The static potential $V(r)$ of the Xe^+ ion is structured as

$$V(\boldsymbol{r}) = -\frac{Z}{r} + V^{\mathrm{DFS}}(r) - V_{1m_{0,1}}(\boldsymbol{r}), \tag{21}$$

where Z is the nuclear charge of the target, $V^{\mathrm{DFS}}(r)$ is the Dirac-Fock-Slater potential where the summation runs over all orbitals (electrons) [33]. The term $V_{1m_{0,1}}(\boldsymbol{r})$ is a hole potential that describes the Coulomb interaction between projectile electron and the orbital $(l,m)=(1m_{0,1})$ in the ion. It is given by

$$V_{1m_{0,1}}(\boldsymbol{r}) = \int |\psi_{5,1}(\boldsymbol{r}')|^2\frac{1}{|\boldsymbol{r}-\boldsymbol{r}'|}\,d\boldsymbol{r}', \tag{22}$$

where $\boldsymbol{r}$ and $\boldsymbol{r}'$ are the position vectors of the projectile and the bound state electrons with respect to the nucleus. $\psi_{5,1}(\boldsymbol{r}')$ is the wave function of the hole state, represented as the antisymmetrized Hartree-Fock wave function expressed in terms of Slater-type orbitals

$$\Phi_{5,1}(r) = R_{5,1}(r) Y_{1m_{0,1}}(\hat{r}), \tag{23}$$

where $Y_{\ell m}(\hat{r})$ are the spherical harmonics and $R_{n,\ell}$ is the radial wave function given by

$$R_{n,\ell}(r) = \sum_{i=1}^{M_{n,\ell}} c_i \frac{1}{\sqrt{(2n_i)!}}(2\xi_i)^{n_i+1/2} r^{n_i-1} e^{-\xi_i r}. \tag{24}$$

The parameters c_i, n_i, ξ_i, and $M_{n,\ell}$ for each of the orbitals are given by Clementi and Roetti [34].

As a result, the hole potential for the $m=0$ and $|m|=1$ vacancy states in the Xe^+ is expressed as

$$\begin{aligned} V_{1,0}(r) &= \int\frac{|P_{5,1}(r')|^2}{r_>}\,dr' + \frac{2}{5}\int |P_{5,1}(r')|^2\frac{(r_<)^2}{(r_>)^3}\,dr' \\ V_{1,1}(r) &= \int\frac{|P_{5,1}(r')|^2}{r_>}\,dr' - \frac{1}{5}\int |P_{5,1}(r')|^2\frac{(r_<)^2}{(r_>)^3}\,dr', \end{aligned} \tag{25}$$

where $P_{n,\ell}(r') = rR_{n,\ell}(r')$ is the radial wave function, for Xe^+ with $n,\ell = 5,1$. Furthermore, $r_< = \min(r,r')$ [$r_> = \max(r,r')$], which represents the smaller (larger) value of r or r'.

It is worth noting that in this work, we ignore the polarization of the hole states by the laser field in the simulations. It was found in previous work [12,35,36] that these effects are negligible for the relatively large electron energies used in the present work. We have verified this by including polarization potential in our simulations and find only small differences compared to the results without polarization potential presented below.

D. The QRS model for HATI

According to the QRS theory [37–39], the detected photoelectron momentum distributions can be factorized as a

product of the momentum distribution of the recolliding wave packet (RWP) and the differential cross section (DCS) for elastic scattering of the returning electron from the parent ion. By defining the HATI photoelectron momentum distribution obtained from the SFA as

$$D^{\mathrm{HATI}}_{\mathrm{SFA2}}(\boldsymbol{p}) = |f_{\mathrm{SFA2}}(\boldsymbol{p})|^2, \tag{26}$$

the QRS model for HATI reads [11]

$$D^{\mathrm{HATI}}_{\mathrm{QRS}}(p,\theta) = W_{\mathrm{SFA2}}(p_r)\frac{d\sigma^{\mathrm{el}}(p_r,\theta_r)}{d\Omega_r}, \tag{27}$$

where $d\sigma^{\mathrm{el}}(p_r,\theta_r)/d\Omega_r$ is the DCS for elastic scattering of the returning electron with the parent ion obtained from Eq. (20). $W_{\mathrm{SFA2}}(p_r)$ is the RWP describing the momentum distribution of the returning electron, which can be obtained by

$$W_{\mathrm{SFA2}}(p_r) = D^{\mathrm{HATI}}_{\mathrm{SFA2}}(p,\theta)\Big/\frac{d\sigma^{\mathrm{el}}_{\mathrm{PWBA}}(p_r,\theta_r)}{d\Omega_r} \tag{28}$$

and is independent of the rescattering angle θ_r. We make the common choice of a large scattering angle $\theta_r = 178^\circ$ [37]. Here $d\sigma^{\mathrm{el}}_{\mathrm{PWBA}}(p_r,\theta_r)/d\Omega_r$ is evaluated using the plane-wave first-order Born approximation, and p, p_r, θ, and θ_r are the detected momentum, rescattering momentum, detected angle, and rescattering angle, respectively.

The detected momentum $\boldsymbol{p}$ and rescattering momentum $\boldsymbol{p}_r$ are related by

$$\boldsymbol{p} = \boldsymbol{p}_r - \boldsymbol{A}_r, \tag{29}$$

where the additional momentum $\boldsymbol{A}_r$ is the vector potential of the laser field at the recollision time. We use the approximation

$$A_r = p_r/1.26, \tag{30}$$

and this relation is determined approximately by solving Newton's equation of motion for an electron in a monochromatic laser field [37]. As a result, the momentum distribution $D^{\mathrm{HATI}}(p,\theta)$ can be understood as a superposition of circles with radii p_r and centers A_r. Tracing the angular distribution on these circles gives access to the DCSs.

E. Experimental method

Experiments have been carried out using the mid-infrared (MIR) laser [40] at the ELI-ALPS laser facility in Szeged, Hungary. The laser provides 40 fs pulses centered around $\lambda = 3100$ nm at a repetition rate of 100 kHz. A pair of wire grid polarizers are used to obtain linearly polarized light with adjustable power. The polarization direction is subsequently adjusted using a motorized broadband half-wave plate (B. Halle). The laser pulses are sent into a stereographic photoelectron time-of-flight spectrometer [41]. The laser is back-focused ($f = 10$ cm) in front of an effusive nozzle injecting Xe gas into the vacuum chamber. Photoelectrons created in the laser focus are detected within a narrow solid angle (≈0.3°) using microchannel plate detectors mounted at a distance of 50 cm, on either side of the spectrometer. Measurements of the photoelectron momentum distribution in the polarization plane are sampled by rotating the polarization axis of the laser and collecting time-of-flight spectra at each angle. The experimental results presented below are symmetrized with respect to reflection at the $p_\perp = 0$ axis. Small asymmetries observed in the raw data indicate a slight ellipticity introduced by the half-wave plate used in the experiment.

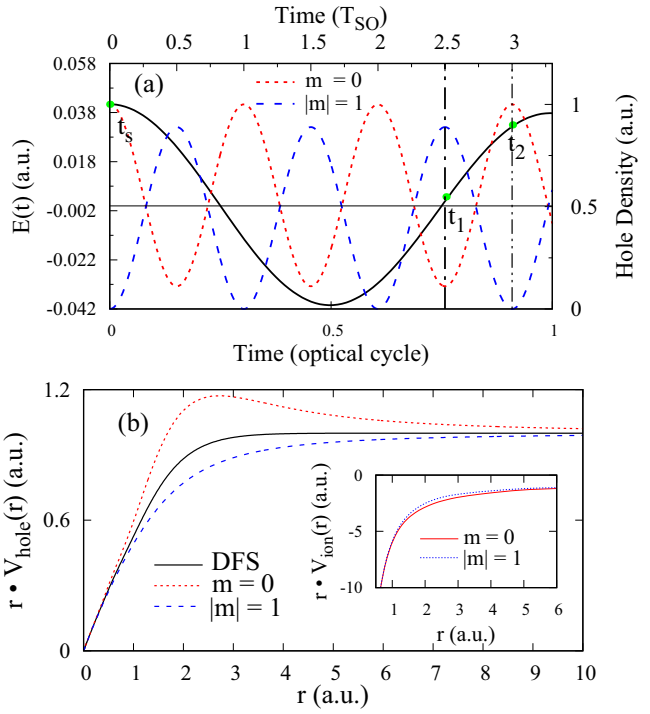

FIG. 1. (a) Schematic of the continuum and bound electron dynamics induced by tunnel ionization. The oscillation of the laser electric field (solid black curve) is compared to the hole population for the $m = 0$ (dotted red curve) and $|m| = 1$ (dotted blue curve) vacancy states. The times $t_1 = 2.5\,T_{\mathrm{SO}}$ and $t_2 = 3.0\,T_{\mathrm{SO}}$ mark times at which the hole populates dominantly the $|m| = 1$ and $m = 0$ states, respectively. (b) Electron-hole potentials (V_{10} and V_{11} for the $m = 0$ and $|m| = 1$ vacancy states of Xe^+, and the Dirac-Fock-Slater potential [33] representing the mean field of all electrons. The inset shows the full scattering potential of the ion, i.e., including the Coulomb term of Eq. (21).

III. RESULTS AND DISCUSSION

Figure 1(a) illustrates the time evolution of the electric field $E(t)$ and the hole-state density in the Xe^+ ion in our experiment. Near the peak of the laser field, around t_s, an electron tunnels from the atom and is subsequently accelerated in the laser field. According to the classical recollision model, the electron returns to the parent ion at a time $t_{1,2}$, roughly $3/4 \pm 1/4$ of an optical cycle after emission, and carries a momentum $p_r(t_r) = -[A(t_s) - A(t_r)]$, where $A(t)$ is the vector potential of the laser field. The travel time $\Delta t = (t_r - t_s)$ of the returning electron corresponds to the delay between electron emission (pump) and recollision (probe). The second clock, corresponding to the spin-orbit wave-packet motion, is also started at t_s. Given the period $T_{\mathrm{SO}} = 3.2$ fs in Xe^+, it is desirable to probe the wave packet at times spanning over 1.6 fs apart. With the wavelength of

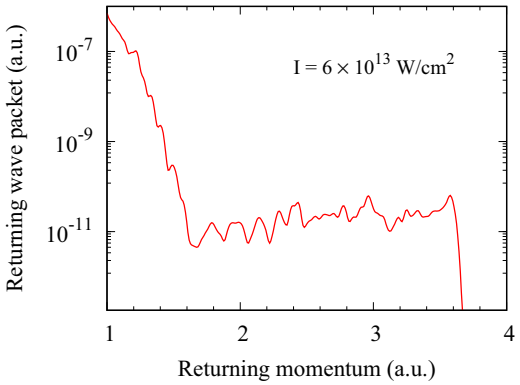

FIG. 2. Momentum distribution of the recolliding wave packet $W_{\mathrm{SFA2}}(p_r)$ for the first returning electron computed from SFA2 for single ionization of Xe by 3100 nm, 40 fs laser pulses at a peak intensity of 6×10^{13} W/cm^2.

3100 nm (optical period $T = 10.5$ fs), we identify the recollision times t_1 and t_2, corresponding to delays of $\Delta t_1 = 2.5T_{\mathrm{SO}} = 8.0$ fs and $\Delta t_2 = 3.0T_{\mathrm{SO}} = 9.6$ fs at which the hole is expected to populate primarily the $|m| = 1$ or $m = 0$ states, respectively.

Figure 1(b) presents the electron-hole potentials weighted by the radial distance for Xe^+ as well for comparison. It can be seen from Fig. 1(b) that the potentials for $m = 0$ and $|m| = 1$ hole states, as well as the Dirac-Fock-Slater potential have the same asymptotic behavior at $r = \infty$. However, as in Eq. (25), it is noticed that the potentials of the $m = 0$ and $|m| = 1$ orbitals differ significantly at around $r = 2$. A similar trend can also be observed for the constructed ion potential in the inset of Fig. 1(b), where the ion potential with the $|m| = 1$ orbital is slightly larger than the ion potential for the $m = 0$ hole state around $r = 2$.

In Fig. 2 we present the momentum distributions of the RWP that account for the weight of contributions from recollisions concerning all energies. The RWPs are extracted from the 2D momentum distributions for HATI of Xe, which were calculated using SFA2. The RWP decreases dramatically at low energies with increasing energy, followed by a plateau in the high-energy region with oscillations until a cutoff is reached.

In Fig. 3 we compare the photoelectron momentum distributions for laser-induced ionization and scattering from Xe obtained experimentally as shown in Fig. 3(a) with the results of our modeling presented in Figs. 3(b) and 3(c). The experimental data exhibit pronounced modulations in the angular distribution of the photoelectrons. These are well reproduced by the QRS results. Despite some discrepancies regarding the electron yield, the good qualitative agreement between experimental and theoretical data along the polarization axis indicates that the DCSs used here are suitable for describing laser-induced rescattering from Xe. However, the simulated momentum distributions for the $m = 0$ and $|m| = 1$ vacancy states are very similar to each other. These small differences cannot be discerned in the experimental data.

Since the computational results for the two hole states are nearly indistinguishable when viewed on the log scale, it is instructive to represent in Fig. 4 the normalized difference of

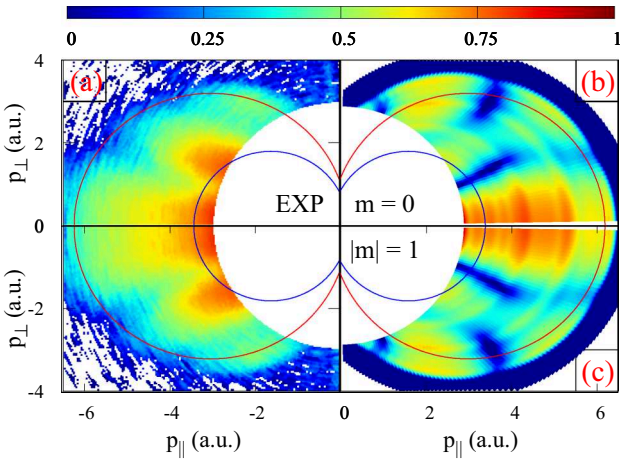

FIG. 3. Left: Measured photoelectron momentum distribution for HATI of xenon using 40-fs laser pulses with a central wavelength of 3100 nm and a peak laser intensity of 6×10^{13} W/cm^2. Right: Results of the QRS calculations for the $m = 0$ (up row) and $|m| = 1$ (below row). The red and blue circles correspond to trajectories with travel times corresponding to $2.5\,T_{\mathrm{SO}}$ ($p_r = 3.4$ a.u.) and $3.0\,T_{\mathrm{SO}}$ ($p_r = 1.8$ a.u.). The central region of the momentum distribution, which is dominated by direct electrons, is removed in order to improve the visibility of the momentum distribution of rescattered electrons.

these spectra, which is defined as

$$A = \frac{D_{m=0} - D_{|m|=1}}{D_{m=0} + D_{|m|=1}}, \tag{31}$$

where $D_{m=0}$ ($D_{|m|=1}$) are the momentum distributions calculated for $m = 0$ ($|m| = 1$). In this way we isolate the

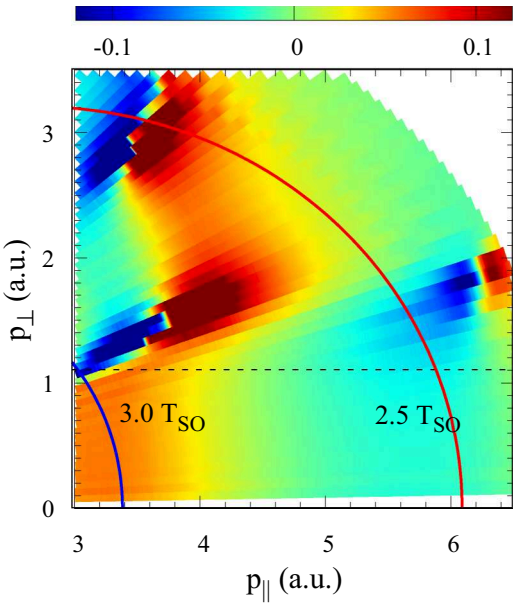

FIG. 4. The normalized difference between the calculated PMD for the recollision of $m = 0$ and $|m| = 1$ states in the Xe^+ ions. The red and blue circular segments correspond to trajectories with travel times corresponding to $2.5\,T_{\mathrm{SO}}$ ($p_r = 3.4$ a.u.) and $3.0\,T_{\mathrm{SO}}$ ($p_r = 1.8$ a.u.).

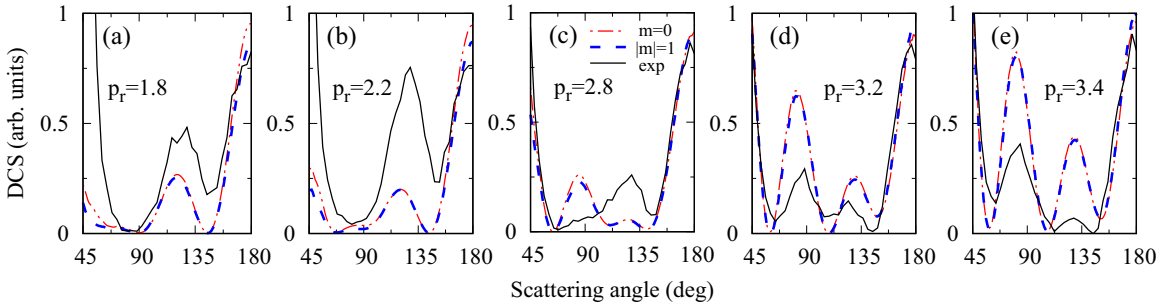

FIG. 5. DCSs for elastic electron scattering from Xe^+ in the $m = 0$ (solid red curve) and $|m| = 1$ (dashed blue curve) hole states for recollision momenta of (a) 1.8 a.u., (b) 2.2 a.u., (c) 2.8 a.u., (d) 3.2 a.u., (e) 3.4 a.u., respectively. The theoretical DCS values are compared to experimental values extracted from the measured photoelectron angular distributions.

differences in the momentum distributions arising from electron scattering from the $m = 0$ and $|m| = 1$ vacancy states. The maxima and minima in this normalized difference plot provide information on where the photoelectron momentum distributions provide contrast between the two vacancy states. Specifically, for small values of $p_\perp$, the maximum positive contrast (more signal for $m = 0$) is obtained around the final momenta of $p_{||} = 3.5$ a.u., while the maximum negative contrast (more signal for $|m| = 1$) is observed at the final momenta of $p_{||} = 6.0$ a.u.. These values coincide with the scattering rings which correspond to the maximum contrast in the population density, indicated as red and blue rings in Figs. 3 and 4, respectively. The numerical results demonstrate that the electron signals due to rescattering from the $m = 0$ and $|m| = 1$ hole states are, in principle, distinguishable. However, the direct measurement of the normalized difference, as presented in Fig. 4, is not at all straightforward. It would require usage of a combination of different laser wavelengths and accurately chosen intensities. Additionally, one could exploit the fact that the spin-orbit period for Kr (6.2 fs) is twice as long as for Xe.

For a quantitative analysis, we present the calculated DCS values for the two hole states in Fig. 5 and compare them to the values extracted from the experimental results at various recollision momenta. The differences observed in Fig. 4 are reflected in the DCS. For example, at low momenta $p_r \sim 2$ a.u., the DCS at 180° is larger for $m = 0$ (cf. red signal in Fig. 4). At higher momenta, $p_r \sim 3$ a.u., however, the DCS at 180° is larger for $|m| = 1$. Moreover, in the intermediate angle range, a marked transition is observed in both experimental and theoretical data: the maximum around 120° observed at $p_r = 2.2$ a.u. is gradually replaced by a maximum around 80° at momenta $p_r \geqslant 3.2$ a.u.. The mismatch observed at $p_r = 2.8$ a.u. is attributed to an uncertainty in the retrieval of the experimental recollision momentum, which is based on the classical recollision model.

While the comparison of the momentum distributions in Fig. 3 indicates a good qualitative agreement between the angular distributions observed in the experimental and numerical results, it is evident that the agreement does not reach the quantitative level necessary to distinguish between the subtle differences observed in the theoretical results for the two hole states. The reasons for the discrepancies between the measured and calculated angular distribution may include several experimental factors, such as the slightly elliptical polarization mentioned above. Moreover, the experimental results are subject to averaging over the spatial intensity distribution in the focus, and the temporal variations of the instantaneous intensity throughout the laser pulse. These effects are not taken into account in the numerical simulations, which are based on the SFA and QRS models. The QRS model used here approximates the temporal variations of the rescattering momentum and vector potential by Eq. (30), which affects the resulting momentum distribution.

IV. CONCLUSIONS AND OUTLOOK

In this work we present a study on the interplay between bound and continuum electron dynamics initiated by strong-field ionization of xenon. Specifically, we investigate whether the ensuing spin-orbit electron dynamics in Xe^+ can be probed through laser-induced electron diffraction. The two-dimensional photoelectron momentum distributions for HATI of Xe are calculated for rescattering from the $m = 0$ and $|m| = 1$ hole states, using the QRS theory. The DCSs of free electrons scattering off the target ion of Xe^+ were calculated with the standard potential scattering theory, and the momentum distributions of returning electrons were evaluated by SFA2. This work represents an initial attempt to experimentally explore valence electron dynamics Xe through LIED. While the numerical results agree with the experimental ones on a qualitative level, they do not reach the quantitative level necessary to distinguish between the rescattering signal from the two hole states. Addressing this challenge likely requires advanced theoretical approaches and more accurate experimental data. If such data become available in the future, an artificial intelligence approach may aid the interpretation of the data and enable the observation of valence electron dynamics by LIED. This intriguing problem underscores the need for future research to address spin-orbit effects during LIED.

ACKNOWLEDGMENTS

The authors acknowledge fruitful discussions with S. Carlström, J. M. Dahlström, and S. Patchkovskii. This research has received funding from the Research School of Advanced Photon Science (RS-APS) at the Helmholtz Institute Jena, Germany and the Deutsche Forschungsgemeinschaft (DFG, German Research Foundation) under the Emmy Noether program, Project No. 437321733.

[1] U. De Giovannini, J. Küpper, and A. Trabattoni, J. Phys. B **56**, 054002 (2023).

[2] K. Amini and J. Biegert, Adv. At. Mol. Opt. Phys. **69**, 163 (2020).

[3] P. B. Corkum, Phys. Rev. Lett. **71**, 1994 (1993).

[4] M. Meckel, D. Comtois, D. Zeidler, A. Staudte, D. Pavićić, H. C. Bandulet, H. Pépin, J. C. Kieffer, R. Dörner, D. M. Villeneuve, and P. B. Corkum, Science **320**, 1478 (2008).

[5] H. Niikura, F. Légaré, R. Hasbani, M. Y. Ivanov, D. M. Villeneuve, and P. B. Corkum, Nature (London) **421**, 826 (2003).

[6] B. Wolter, M. G. Pullen, A.-T. Le, M. Baudisch, K. Doblhoff-Dier, A. Senftleben, M. Hemmer, C. D. Schröter, J. Ullrich, T. Pfeifer *et al.*, Science **354**, 308 (2016).

[7] C. I. Blaga, J. Xu, A. D. DiChiara, E. Sistrunk, K. Zhang, P. Agostini, T. A. Miller, L. F. DiMauro, and C. D. Lin, Nature (London) **483**, 194 (2012).

[8] B. Walker, B. Sheehy, K. C. Kulander, and L. F. DiMauro, Phys. Rev. Lett. **77**, 5031 (1996).

[9] M. Lein, J. P. Marangos, and P. L. Knight, Phys. Rev. A **66**, 051404(R) (2002).

[10] A. Sanchez, K. Amini, S.-J. Wang, T. Steinle, B. Belsa, J. Danek, A. T. Le, X. Liu, R. Moshammer, T. Pfeifer *et al.*, Nat. Commun. **12**, 1520 (2021).

[11] Z. Chen, A. T. Le, T. Morishita, and C. D. Lin, J. Phys. B **42**, 061001 (2009).

[12] S. N. Nahar and J. M. Wadehra, Phys. Rev. A **35**, 2051 (1987).

[13] N. Rohringer and R. Santra, Phys. Rev. A **79**, 053402 (2009).

[14] I. Linert, B. Mielewska, G. C. King, and M. Zubek, Phys. Rev. A **74**, 042701 (2006).

[15] S. Baker, J. S. Robinson, C. A. Haworth, H. Teng, R. A. Smith, C. C. Chirilă, M. Lein, J. W. G. Tisch, and J. P. Marangos, Science **312**, 424 (2006).

[16] D. Shafir, B. Fabre, J. Higuet, H. Soifer, M. Dagan, D. Descamps, E. Mével, S. Petit, H. J. Wörner, B. Pons *et al.*, Phys. Rev. Lett. **108**, 203001 (2012).

[17] S. Haessler, J. Caillat, W. Boutu, C. Giovanetti-Teixeira, T. Ruchon, T. Auguste, Z. Diveki, P. Breger, A. Maquet, B. Carré *et al.*, Nat. Phys. **6**, 200 (2010).

[18] A. Shiner, B. Schmidt, C. Trallero-Herrero, H. J. Wörner, S. Patchkovskii, P. B. Corkum, J-C. Kieffer, F. Légaré, and D. M. Villeneuve, Nat. Phys. **7**, 464 (2011).

[19] R. de Nalda, E. Heesel, M. Lein, N. Hay, R. Velotta, E. Springate, M. Castillejo, and J. P. Marangos, Phys. Rev. A **69**, 031804(R) (2004).

[20] D. G. Lappas and J. P. Marangos, J. Phys. B **33**, 4679 (2000).

[21] T. Ichibayashi and K. Tanimura, Phys. Rev. Lett. **102**, 087403 (2009).

[22] T. Ichibayashi, S. Tanaka, J. Kanasaki, K. Tanimura, and T. Fauster, Phys. Rev. B **84**, 235210 (2011).

[23] H. J. Wörner and P. B. Corkum, J. Phys. B **44**, 041001 (2011).

[24] E. Goulielmakis, Z. Loh, A. Wirth, R. Santra, N. Rohringer, V. S. Yakovlev, S. Zherebtsov, T. Pfeifer, A. M. Azzeer, M. F. Kling *et al.*, Nature (London) **466**, 739 (2010).

[25] A. Fleischer, H. J. Wörner, L. Arissian, L. R. Liu, M. Meckel, A. Rippert, R. Dörner, D. M. Villeneuve, P. B. Corkum, and A. Staudte, Phys. Rev. Lett. **107**, 113003 (2011).

[26] P. C. Fechner and H. Helm, Phys. Chem. Chem. Phys. **16**, 453 (2014).

[27] M. Kübel, Z. Dube, A. Yu. Naumov, D. M. Villeneuve, P. B. Corkum, and A. Staudte, Nat. Commun. **10**, 1042 (2019).

[28] G. A. Stewart, P. Hoerner, D. A. Debrah, S. K. Lee, and H. B. Schlegel, and W. Li, Phys. Rev. Lett. **130**, 083202 (2023).

[29] Z. Chen, T. Morishita, A.-T. Le, and C. D. Lin, Phys. Rev. A **76**, 043402 (2007).

[30] D. F. Dar, B. Minneker, and S. Fritzsche, Phys. Rev. A **107**, 053102 (2023).

[31] X. M. Tong and C. D. Lin, J. Phys. B **38**, 2593 (2005).

[32] C. J. Joachain, *Quantum Collision Theory* (North-Holland, Netherlands, 1975).

[33] S. Fritzsche, Comput. Phys. Commun. **240**, 1 (2019).

[34] E. Clementi and C. Roetti, At. Data Nucl. Data Tables **14**, 177 (1974).

[35] Z.-J. Chen and D.-D. Cui, Chin. Phys. B **27**, 053403 (2018).

[36] P. Soldán, E. P. F. Lee, and T. G. Wright, Phys. Chem. Chem. Phys. **3**, 4661 (2001).

[37] Z. Chen, A. T. Le, T. Morishita, and C. D. Lin, Phys. Rev. A **79**, 033409 (2009).

[38] Z. Chen, Y. Liang, and C. D. Lin, Phys. Rev. Lett. **104**, 253201 (2010).

[39] F. Liu, S. Li, Z. Chen, B. Böning, and S. Fritzsche, Phys. Rev. A **106**, 043120 (2022).

[40] M. Kurucz, R. Flender, L. Haizer, R. S. Nagymihaly, W. Cho, K. T. Kim, S. Toth, E. Cormier, and B. Kiss, Opt. Commun. **472**, 126035 (2020).

[41] M. Kübel, P. Wustelt, Y. Zhang, S. Skruszewicz, D. Hoff, D. Würzler, H. Kang, D. Zille, D. Adolph, G. G. Paulus *et al.*, Phys. Rev. Lett. **126**, 113201 (2021).